Compact Design of a Hydraulic Driving Robot for Intraoperative MRI-Guided Bilateral Stereotactic Neurosurgery

Ziyan Guo, Ziyang Dong, Kit-Hang Lee, Chim Lee Cheung, Hing-Choi Fu, Justin D.L. Ho, Haokun He, Wai-Sang Poon, Danny Tat-Ming Chan, and Ka-Wai Kwok

***Abstract*—In this letter, we present an intraoperative magnetic resonance imaging (MRI)-guided robot for bilateral stereotactic procedures. Its compact design enables robot's operation within the constrained space of standard imaging head coil. magnetic resonance (MR) safe and high-performance hydraulic transmissions are incorporated. A maximum stiffness coefficient of 24.35 N/mm can be achieved with transmission fluid preloaded at 2 bar. Sufficient targeting accuracy (average within ≤1.73 mm) has been demonstrated in a simulated needle insertion task of deep brain stimulation. A novel MR-based *wireless* tracking technique is adopted. It is capable of offering real-time and continuous (30–40 Hz) three-dimensional (3-D) localization of robotic instrument under the proper MR tracking sequence. It outperforms the conventional method of using low-contrast passive fiducials that can only be revealed in the MR image domain. Two *wireless* tracking units/markers are integrated with the robot, which are two miniaturized coil circuits in size of $1.5 \times 5 \times 0.2$ mm^3, fabricated on flexible thin films. A navigation test was performed under the standard MRI settings in order to visualize the 3-D localization of the robotic instrument. MRI compatibility test was also carried out to prove the minimal interference to MR images of the presented hydraulic robotic platform.**

***Index Terms*—MRI-guided interventions, stereotactic neurosurgery, surgical robotics.**

I. Introduction

STEREOTAXY is a technique that can locate targets of surgical interest using an external coordinate system as reference. Its application in functional neurosurgery mostly aims to treat a variety of movement disorders (e.g., Parkinson's disease (PD) and dystonia), psychiatric abnormalities and epilepsy. PD alone is the second most common disease of the nervous system after Alzheimer's disease, and is projected to affect over 8.7 million people worldwide by 2030 [1]. Deep brain stimulation (DBS) is one of the common stereotactic procedures, which is a surgical treatment for debilitating motor symptoms of PD and dystonia. *Two* long (e.g., 300 mm) slender (≈Ø1.3 mm) DBS needles will be individually guided by a stereotactic frame and inserted through burr holes (≤ Ø14 mm.) into the patient's skull. Stimulation electrodes embedded at the tip of needle will then be implanted to the deep brain areas of interest, thus delivering programmed electrical impulses.

Although the standard workflow of stereotactic neurosurgery has been established for over half a century, the operation still remains challenging due to its complicated workflow and high demand for surgical accuracy. The average recorded error of 2–3 mm is just barely tolerable [2]. Stereotactic navigation could be further complicated by substantial deformation of intracranial contents, namely "brain shift", which occurs inevitably after craniotomy. The shift is mainly caused by gravity, cerebrospinal fluid (CSF) leakage, anesthesia and surgical manipulation. It could induce misalignment (as large as 10–30 mm [3]) of the pre-operative (pre-op) planning path, aiming beyond the actual target. In conventional DBS guided by fluoroscopy/computed tomography (CT), microelectrode recording (MER) is adopted frequently to confirm the acceptable placement of electrodes while assessing the corresponding symptoms with the awake patient under local anesthesia. These complications pose increasing expectation on intra-operative (intra-op) magnetic resonance imaging (MRI)-guided stereotaxy. Unlike fluoroscopy/CT, MRI can directly visualize the critical brain structures and targets of interest (e.g., subthalamic nucleus (STN), globus pallidus interna (GPi) or ventral intermediate nucleus).

Currently, there are very limited choices of MR safe stereotactic systems [2], [4] (e.g., NexFrame, Medtronic Inc., USA and ClearPoint, MRI Interventions Inc., USA). They generally require intensive manual adjustment of the stereotactic frame, and the patient to be transferred in-and-out of the scanner bore. This eventually disrupts the workflow. To this end, MR safe/conditional robotic platforms have been introduced. An FDA approved prototype, SYMBIS (formerly called NeuroArmg, IMRIS Inc., Canada), is an MRI-compatible robot built

Manuscript received September 10, 2017; accepted February 2, 2018. Date of publication March 9, 2018; date of current version March 29, 2018. This letter was recommended for publication by Associate Editor T. Haidegger and Editor K. Masamune upon evaluation of the reviewers' comments. This work was supported in part by Signate Life Sciences Limited, in part by the Croucher Foundation, and in part by the Research Grants Council of Hong Kong (Refs. 27209515, 17227616, and 17202317). *(Corresponding author: Ka-Wai Kwok.)*

Z. Guo, Z. Dong, K. H. Lee, C. L. Cheung, H. C. Fu, J. D. L. Ho, H. He, and K. W. Kwok are with the Department of Mechanical Engineering, The University of Hong Kong, Hong Kong (e-mail: guoziyan@connect.hku.hk; ziyang.dong.matthew@gmail.com; briankhl@hku.hk; zardchim@hku.hk; sk001031@gmail.com; jdlho@connect.hku.hk; hkhe0812@outlook.com; kwokkw@hku.hk).

W. S. Poon and D. T. M. Chan are with the Division of Neurosurgery, Prince of Wales Hospital, Hong Kong (e-mail: wpoon@cuhk.edu.hk; tmdanny@surgery.cuhk.edu.hk).

Digital Object Identifier 10.1109/LRA.2018.2814637

predominantly for tele-operated microsurgery, and only one of its robot arms capable of MRI-guided stereotaxy [5]. This MRI-compatible robot arm is actuated by piezoelectric motors and the robot body is made of titanium or polyetheretherketone (PEEK) to ensure its MRI compatibility [6]. It can be mounted on the magnet bore, providing constant spatial relation with the magnet isocenter and the patient's anatomy. However, it creates a large footprint in the surgical theater while transferring the intra-op scanner in-and-out for each imaging update, introducing much procedural complexity.

Neuroblate (Monteris Medical Inc., USA) is a robotic probe with 2 degrees of freedom (DoFs) (rotation and translation) driven by piezoelectric motors for stereotactic laser ablation [7]. The probe can be passively oriented by AXiiiS stereotactic miniframe, which consists of a ball-socket, three legs and a 360° directional interface. Real-time MR-thermometry data can be provided to ensure safe ablation boundaries from surrounding structures [8]. For multiple surgical paths, the patient will be transferred back to the operating theater to remove the probe, relocate/realign the frame and create new craniotomy.

A research prototype developed by Fischer *et al.* [9], [10] towards needle-based neural interventions was reported. The robot is kinematically equivalent with the conventional stereotactic frame (e.g., Leksell frame, Elekta AB, Sweden) and is actuated by piezoelectric motors as well. A control system for these motors is specially designed to allow the simultaneous MR imaging and robot motion, ensuring sufficient image quality for surgical guidance. The robot can be fixed on the surgical table. However, to complete the whole procedure inside the MRI scanner, it may require a specialized MRI head coil or scanner with larger spatial clearance for robot's operation (1.5/3 T MRI scanners usually with inner diameter of Ø600 mm).

Compactness and MRI compatibility are two crucial issues regarding the feasibility and adaptability of robots in the regular hospital setup. Very few robotic platforms can fit with the MRI head coil, and also operate during continuous imaging without degrading the image quality. None of the aforementioned platforms can accommodate the trend towards *bilateral* DBS, which becomes the most popular approach for PD [11]. In addition, positional tracking in almost all of them is conducted using either optical tracker or passive MR fiducials, which introduces significant error while registering the robot coordinates with the imaging ones [12]. MR-based tracking involves tiny coils (e.g., Ø3 $\times$ 8 mm^3 [13]) designed to resonate with MR Larmor frequency. It enables real-time localization of robotic instruments. In general, there is no robotic system for functional neurosurgery incorporated with MR safe actuation and MR-based tracking, capable of performing stereotactic manipulation inside the MRI bore [14]. Therefore, the contributions of our work in this letter can be well-differentiated as follows:

i) Development of the *first* intra-op MRI-guided robot capable of performing *bilateral* neuro-stereotaxy based on a single anchorage on the patient skull. Navigation for both bilateral targets can be performed independently and simultaneously.
ii) A light-weight (145.4 g) and compact (110.6 $\times$ 206.8 $\times$ 33.2 mm^3) robot designed to operate within the confined workspace of an MR imaging head coil. It is also actuated by a set of high-performance hydraulic transmissions which are MR safe/induce minimal imaging artifacts.
iii) MRI-guided navigation incorporated with *wireless* MR-based tracking coil units, offering real-time positional feedback directly in MR image coordinates. This avoids any process of offline registration between coordinates of the tracking and imaging space.

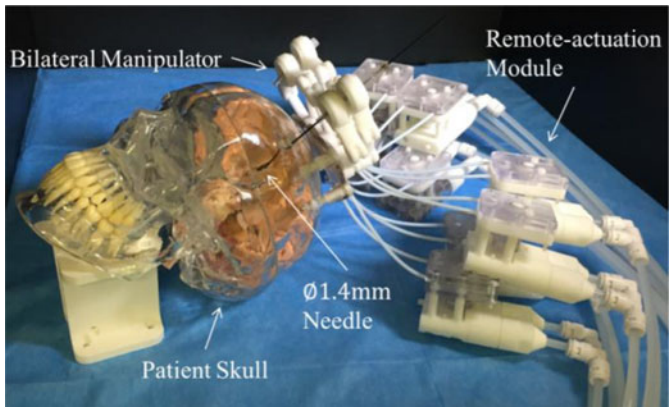

Fig. 1. Slave module of the proposed MR safe robot for intra-op MRI-guided bilateral stereotactic procedures.

II. Methodology

The proposed robot (Fig. 1) is designed to perform bilateral instrument navigation in particular for the use of intra-op MRI-guided DBS. Anatomical target, STN, is ellipsoid alike and typically situated in the deep region of brain (90 mm beneath the skull) [15]. Accuracy of the electrode placement must be less than 3 mm in order to maintain optimal stimulation effect. The robot design criteria are stated in the following section.

A. Robot Design Criteria

Two burr holes are created on the skull for the procedure. The proposed robot consists of two manipulators (Fig. 2) which will be mounted on the middle line of the two burr holes. Each provides 4-DoF manipulation of the instrument access to the corresponding hole, including pitch, roll, and offsets along X-Y plane above the skull surface. This facilitates alignment of the instrument with the desired straight-line trajectory to the STN. Fine adjustments ranged in either X or Y direction of $\pm$2.5 mm, and pitch angle of $\pm$33°, and roll angle of $\pm$26° are more than sufficient to cover the required workspace in many cases [15].

Provided with the intra-op 3-dimensional (3D) MR images (e.g., acquired by gadolinium-enhanced T1-weighted volumetric scan), surgeons can identify the mid-commissural point (MCP), as well as the STN targets based on the anterior commissure-posterior commissure (AC-PC) line, thereby determining the desired entry point and insertion path to the target. Note that the robot must be operated in the deep brain target coordinates frame, which is defined on the basis of the AC-PC

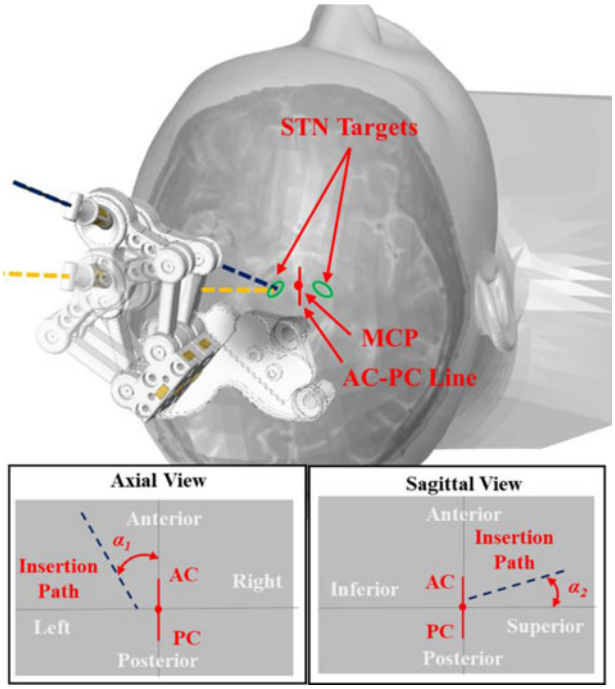

Fig. 2. A single manipulator shown with two possible configurations. Boundaries of STN targets highlighted in green, which could be revealed by T2-weighted MRI. The insertion path is the pre-operatively planned trajectory. Its angular inclinations (α_1 and α_2) and projection at axial/sagittal planes are shown in the block at lower left and lower right corner, respectively.

line, such that around 3–4 mm posterior, 5–6 mm inferior and 12 mm lateral with respect to (w.r.t.) the MCP (Fig. 2) [16].

To facilitate the bilateral stereotactic manipulation, the robot is designed: **i)** to be compact so that the robot body can be fixed on patient's skull properly within the head coil; **ii)** to enable automatic trajectory planning and instrument alignment; **iii)** to perform bilateral manipulation independently; **iv)** to fulfill the MRI compatibility upon ASTM F2503-13 standard [17], which defines MR safety, by ensuring no conductive, metallic or magnetic components are involved in the robotic platform.

B. Master-Slave Actuation Mechanism

Short-tendon-driven design is adopted with the aim to reach stringent criteria, in terms of not only the spatial constraints imposed by the head coil, but also the weight that may cause discomfort to the patient. Fig. 3 shows a slave manipulator in the MRI room, which is wired with a pair of hydraulic transmission units connecting with the other pair in the control room. Such a compact design of the slave can minimize the motion inertia and facilitate manipulation flexibility across the constrained workspace. It is still capable of applying a promising level of torque/force generated by the hydraulic motor. At this stage, the design is mostly prototyped by 3D-printed components made of polymers (VeroClear, Stratasys Inc., USA).

For a 1-DoF actuation, as depicted in Fig. 3, the manipulator base joint and the hydraulic units are separated by $<$200 mm. They are connected with one loop of thin (Ø0.16 mm) tendons (Dyneema polyethylene (PE), Tokushima Inc., Japan) tightly channeled through the Teflon sheaths (outer/inner diameter: Ø2/0.5 mm). The sheath material is axially-incompressible to prevent sudden/excessive pulling force applied on the skull. It also supports the route of tendon with sufficient pliability even under the high tensile strength. The tendon-sheath friction is reduced by proper lubrication. Two idlers are used to pre-load the tension in order to reduce any mechanical backlash.

The master (in control room) and slave (in MRI room) actuation system consists of two identical pinion-and-rack units to transfer the linear motion to rotary (Fig. 3). The hydraulic power originates from an electric stepper motor (57BYG250-80, Hongfuda Inc., China) and is transmitted via a pair of semi-rigid long pipes made of nylon. The length of this pipe pair is 8m. The outer and inner diameters of the pipes are, respectively, 6 mm and 4 mm. These design parameters are of importance to the performance of transmission dynamics. It is suggested [18] that using pipes with shorter length and larger diameter can reduce the fluid friction, transmission latency and energy loss. The pipes are filled with incompressible liquid (e.g., water) and are passed through the waveguide in between two rooms. Note that the liquid pressure can be pre-loaded to push the piston towards the pinion-and-rack gear, keeping their teeth in steady contact without backlash.

Rolling-diaphragms (Ø15 mm, MCS3014MOP, FEFA Inc., Germany) are used to seal the cylinders with negligible sliding friction during transmission. Let alone the pneumatic actuation approaches [19]–[21], it is worth noting that the resultant transmission response and power efficiency is already ensured to outperform the use of conventional hydraulic sealing with O-rings, of which the sliding friction is severe [22]. The wall of this rubber diaphragm is reinforced by fabric to withstand the high fluid pressure [23]. Its maximum linear stroke is 20 mm, driving the rotary motion of pinion at most by 100.6°, corresponding to the 201.2° rotation at the base joint.

C. Bilateral Manipulator Design

The CAD model and components of the proposed robotic manipulator are illustrated in Fig. 4(a). Parallel mechanisms possess advantages in positioning accuracy and stiffness. Large workspace-to-footprint ratio of a five-bar planar parallel mechanism [24], [25] has also been discussed. Its planar position is controlled by two actuated rotational joints and three passive ones, namely RRRRR mechanism. The above advantages lead to our design of two 4-DoF double-layer five-bar-linkage manipulators in bilateral setting.

The manipulator mainly consists of rigid arms, four housings and a mounting base fixed with the skull via four bone screws, two for each side. All four anchorage sites are away from the sagittal suture to avoid the possible trauma to the critical structures underneath. In the current prototype, lowest surface of the arms is 20–30 mm above the burr hole, depending on the patient-specific skull curvature and its anchorage site (Fig. 4(b)). This exposure space at the entry point is reserved for surgeon's observation. For versatility, the mounting base can be tailor-made for patient based on the pre-op images. All the housings are rigidly accommodated on the mounting base. Slots on the surface are reserved for the attachment of registration markers. Passages

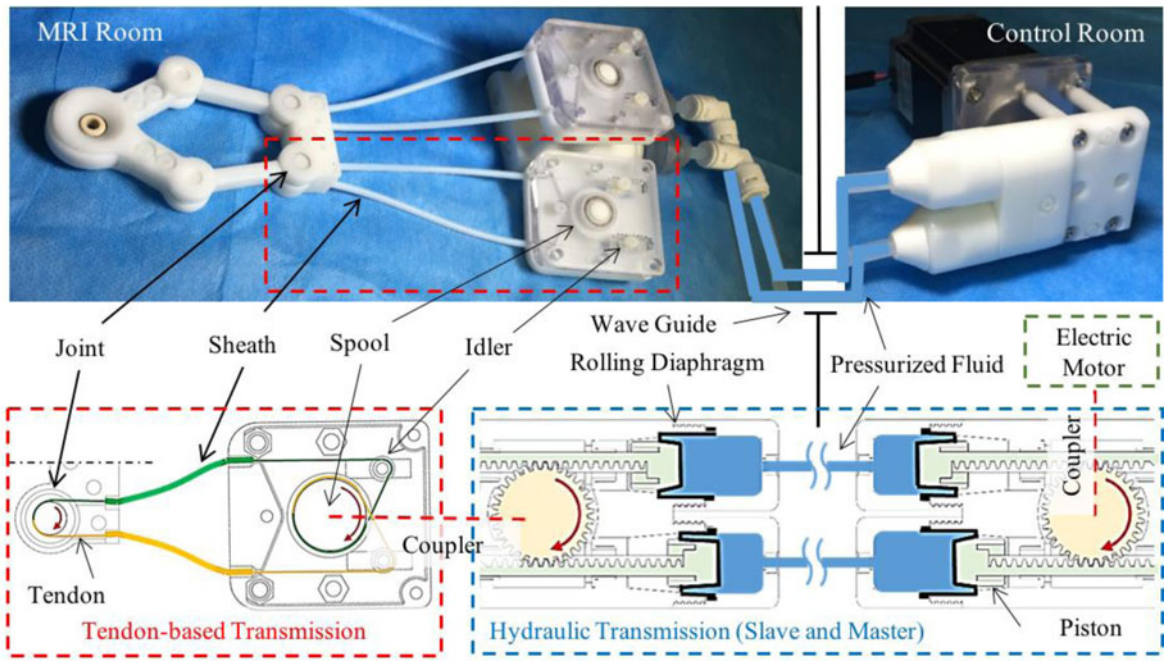

Fig. 3. Key components and schematic diagram of a 1-DoF actuation design.

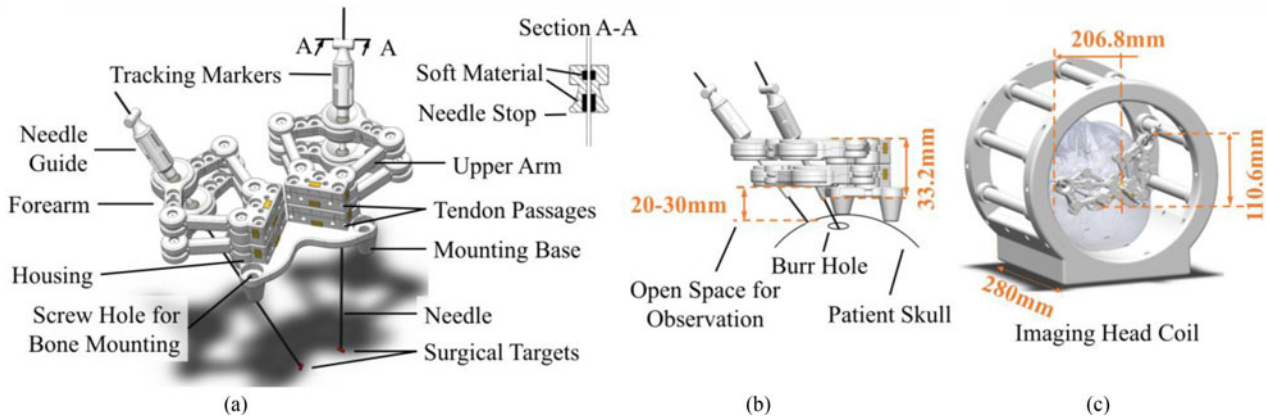

Fig. 4. (a) CAD model showing the key components of our bilateral stereotactic manipulators. (b) Lower layer of the manipulator positioned about 30mm above the skull surface, which remains the sufficient space for ease of observation around the burr hole. (c) Overall dimensions observed, which demonstrates the design is so compact that two (bilateral) manipulators attached on skull can be fully stretched in two extreme configurations within the confined space of a Siemens-style mock head coil (inner diameter Ø265mm).

are also created to allow fixture of the sheath's end for better tendon routing. The revolute joints inside the housing can be therefore actuated by the tendons. Two ball joints (igus Inc., Germany) are incorporated at the distal end of the forearms. A needle guide is oriented by these two joints, and axially fixed with the upper one. In prior to inserting the needle through the cannula held by both end-effectors of the double-layer manipulators, the allowable insertion depth is preset by the needle stop. Soft material is also embedded inside the cannula/needle stop so as to limit the needle linear motion by inducing the sliding friction.

D. Forward and Inverse Kinematics

Fig. 5 depicts the kinematic diagram of one double-layer manipulator. Two coordinate frames Ψ_O and Ψ_E are defined at the housing base and needle tip, respectively. The cannula is connected by two passive joints J_{u5} and J_{l5} from upper and lower layers, respectively. Its pose can be manipulated by independent (X-Y) planar motion of the upper and lower layers containing the points p_{uk} and p_{lk} $(k = 1, \cdots, 5)$, respectively. Such points denote the 2D coordinate of their corresponding joints J_{uk} and J_{lk} $(k = 1, \cdots, 5)$, which can be solved by the following equation sets:

$$\begin{cases} \|p_{u3} - p_{u5}\| = l_f \\ \|p_{u4} - p_{u5}\| = l_f \end{cases} \text{and} \begin{cases} \|p_{l3} - p_{l5}\| = l_f \\ \|p_{l4} - p_{l5}\| = l_f \end{cases} \quad (1)$$

Horizontal offset a separating two actuated joints (i.e., J_{u1} and J_{u2} or J_{l1} and J_{l2}) is 25 mm, while the vertical offset b of two layers is 16 mm. The array of actuated joint can be defined as $q = [q_1, q_2, q_3, q_4]^T$. Therefore, the angular ranges of active

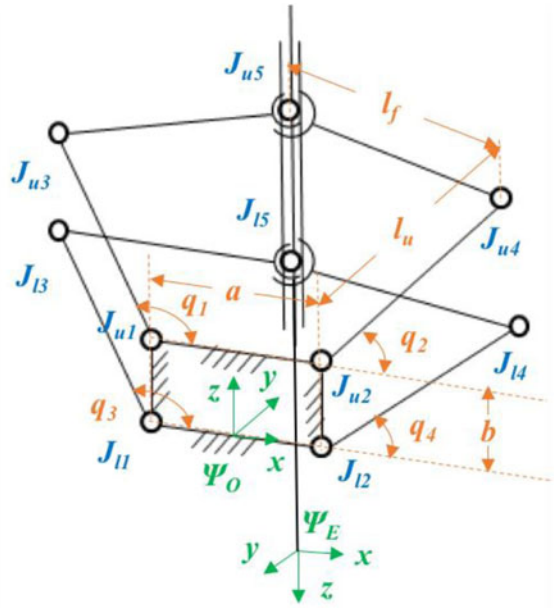

Fig. 5. Kinematic diagram of a single manipulator with coordinate frames Ψ_O and Ψ_E defined at the housing base and the needle tip, respectively.

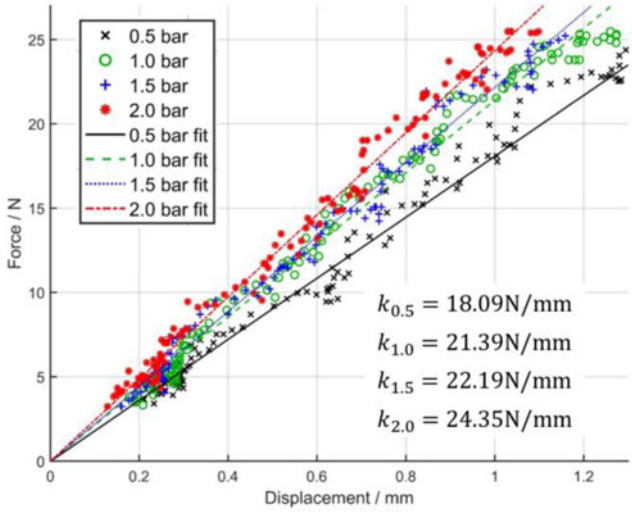

Fig. 6. Force-displacement diagram showing the transmission stiffness of the actuation module at four levels (0.5, 1, 1.5 and 2 bars) of pressure pre-loaded on the transmission liquid.

joints J_{u1}, J_{l1} are corresponding to $q_1, q_3 \in [29.7^\circ, 195.3^\circ]$; for joints J_{u2}, J_{l2} are $q_2, q_4 \in [-15.3^\circ, 150.3^\circ]$. The length of two proximal links (upper arms) l_u is 40 mm; for two distal links (forearms) l_f is 35 mm. Two types of singularities can be found in this five-bar linkage mechanism [26]. The first type takes place when forearms are collinear (e.g., joints J_{l3}, J_{l4}, J_{l5} are in one line), and the second one appears only when arms are fully stretched. To prevent collineation of the pair of forearms, a mechanical limit on the relative rotation is adopted. For instance, joint J_{l5} will always locate outside quadrangle area of $J_{l1}J_{l2}J_{l3}J_{l4}$. To resolve the forward kinematics, the needle's orientation can be denoted by the unit $\vec{r}$ as:

$$\vec{r} = \frac{p_{l5} - p_{u5}}{\|p_{l5} - p_{u5}\|} \tag{2}$$

Assume the insertion depths, d_u and d_l, are defined as the linear distances from joints J_{u5} and J_{l5}, respectively, to the target. The position of needle tip p_t, acting as the ultimate end effector of both manipulators can be calculated:

$$p_t = p_{u5} + d_u \cdot \vec{r} \tag{3}$$

To find the four actuated joint angles $q = [q_1, q_2, q_3, q_4]^T$ based on the desired needle pose w.r.t. the MR image coordinates, co-registration between the robot and image coordinate system is required. Again, the planned parameters (i.e., p_t and $\vec{r}$) can be defined in Ψ_O. Coordinates p_{u5}, p_{l5} can be found by calculating the crossing points of needle and two layers using the line equations:

$$p_{u5} = p_t - d_u \cdot \vec{r} \text{ and } p_{l5} = p_t - d_l \cdot \vec{r} \tag{4}$$

Note that coordinates p_{u5} and p_{l5} belong to triangle $\Delta J_{u1}J_{u3}J_{u5}$ and $\Delta J_{l1}J_{l3}J_{l5}$, respectively. Then, angle $\angle J_{u3}J_{u1}J_{u5}$ and $\angle J_{u4}J_{u2}J_{u5}$ (denoted as θ_{u1}, θ_{u2}) can be solved using cosine laws, respectively, in triangle $\Delta J_{u1}J_{u3}J_{u5}$ and $\Delta J_{u2}J_{u4}J_{u5}$:

$$l_f^2 = l_u^2 + \|p_{u5} - p_{u1}\|^2 - 2l_u \|p_{u5} - p_{u1}\| \cos\theta_{u1} \tag{5}$$

$$l_f^2 = l_u^2 + \|p_{u2} - p_{u5}\|^2 - 2l_u \|p_{u2} - p_{u5}\| \cos\theta_{u2} \tag{6}$$

Angles $\angle J_{u2}J_{u1}J_{u5}$ and $\angle J_{u5}J_{u2}J_{u1}$ (denoted as α_{u1} and α_{u2}) can be obtained similarly in triangle $\Delta J_{u1}J_{u2}J_{u5}$. To avoid the second type of singularity, joint J_{u3}, J_{u4} should be always positioned beyond triangle $\Delta J_{u1}J_{u2}J_{u5}$ such that, $q_1 = \theta_{u1} + \alpha_{u1}$ and $q_2 = \pi - (\theta_{u2} + \alpha_{u2})$. The other actuation angles q_3, q_4 can be solved based on the similar process.

III. Experiments and Results

A. Transmission Stiffness

One of the primary factors which determines the system's capability to resist external disturbance is the stiffness of the hydraulic transmission presented. An iterative test was conducted on a 1-DoF actuation, i.e., from the master side to the manipulator's base joint. The upper arms of manipulator were fixed such that rotation of the actuated joint was constrained properly. 10m long pipes filled with distilled water were used to connect both the master-and-slave hydraulic units. The master unit was actuated by an electrical DC motor that provided with 500 encoding pulses feedback. A torque sensor (HLT131, Hualiteng Technology Co. Ltd., China) with 5 mNm sensitivity was used to measure the external load. The tests were performed repeatedly (10 cycles) under the bi-directional load. The transmission fluid in the pipes was preloaded at 0.5, 1.0, 1.5 and 2.0 bar in order to investigate the transmission stiffness varying with different fluid pressure levels. The external loads were gradually increased, while recording the corresponding piston displacements.

The force-displacement diagram (Fig. 6) shows the increasing trend of transmission stiffness with higher fluid pressure pre-loaded. The data was linearly fitted using least-square

TABLE I
NEEDLE TARGETING ACCURACY TEST

	Needle tip		Normal to the needle	
Accuracy (mm)	Left	Right	Left	Right
	1.73 ± 0.75	**1.21 ± 0.63**	**1.61 ± 0.72**	**1.15 ± 0.62**

regression, which indicated the maximum stiffness coefficient can reach 24.35 N/mm under 2bar pre-loaded pressure. The interaction force between instrument and brain tissue is generally less than 0.8 N [5], [27]. It is indicated that the proposed hydraulic transmission is stiff enough to transmit motion for precise tissue manipulation. Compliance in the transmission can be attributed to three major factors: i) stretching of the diaphragms, ii) deformation of the plastic structural components, and iii) bulging in cross-sectional area of the pipes. To further increase the transmission stiffness, components can be machined by materials with higher rigidity, e.g., polyoxymethylene. Thus, the minimal structural deformation under loading can be ensured. Previous studies [18] have suggested shorter pipes can also contribute to higher stiffness, as well as lower fluid inertia and friction.

B. Needle Targeting Accuracy

An EM positional tracking system (Aurora, NDI Medical, Canada) was used to measure the 3D coordinates of any point defined in the experimental setup. Ten points were simulated as the STN targets, five at each side on a plastic plate. They were roughly 100 mm below the lower-layer of manipulators, which was a typical depth of stereotactic target beneath the human skull. These measured targets coordinates were registered with the robot coordinate system. A phantom needle with similar diameter (Ø1.4 mm) to a DBS cannula was used. A 6-DoF coil sensor was fixed at the needle tip.

Configurations of the robot and needle guide, along with the needle insertion depth, were measured and calculated online. Once aiming at the target point, the needle was then inserted manually. Such trial for each point was repeated 10 times. 100 trials were conducted in total. This targeting task was performed closely to the tracking system, and measurements were taken when the 6-DoF sensor was at rest. These measurements were repeated 500 times at each static location. The average of these 500 measurements was used in the error analysis. Not only was the proximal distance from needle tip to the target measured, but also the distance from the target to the needle axis. The targeting accuracy was quantified by the mean error and its standard deviation (Table I). The error is generally less than 2 mm, and its variation also smaller than 1 mm. This accuracy is comparable to the current stereotaxy practice [2]. Future work in robot calibration and structural rigidity enhancement may further improve this targeting performance.

C. MR-Based Tracking Test

MR-based *wireless* tracking is first introduced to such robotic stereotaxy. It possesses several advantages over the conventional

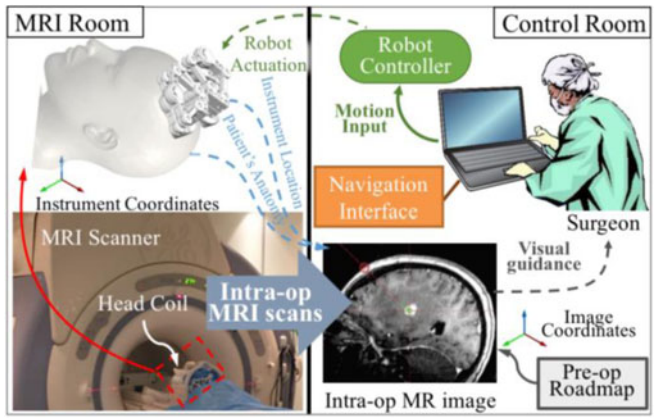

Fig. 7. System schematic of the MRI-guided robot-assisted stereotaxy.

TABLE II
MRI SCAN PARAMETERS

	w/o needle inserted	*w/* needle inserted	SNR test
FOV (mm)	240 × 240	240 × 240	280 × 280
Matrix	256 × 256	256 × 256	256 × 256
Acquisition	FSPGR	FSPGR	T2-FSE
TR (ms)	68.0	68.0	2000.0
TE (ms)	2.8	2.8	76.8
Flip angle (°)	10	10	90

passive tracking [28], [29], in which the real-time and automatic localization cannot be made reliable due to their limited signal contrast to the background. The use of passive tracking could also be time-consuming as visualization of the markers takes place after 2D image reconstruction. The proposed *wireless* and *miniaturized* marker can act as an RF receiver to pick up the MR gradient signal along three principal scanning directions, as well as an inductor to resonate with the signal transmitted to the MRI scanner receiver [30]–[32]. Without the need for image reconstruction, they can be rapidly localized using 1D projection techniques [13].

The navigation test was carried out under MRI environment. It simulated the conceptual system setup for MRI-guided robotic stereotaxy, as in Fig. 7. To better simulate the surgical scenario, the robot was mounted on the skull model that would be placed and scanned inside a head coil. To reveal the brain phantom in MR image, the "brain" was fabricated and made of agar gel (Biosharp Inc., China) to enhance the image contrast for needle targeting. The two films of MR coil circuits ($1.5 \times 5 \times 0.2$ mm^3) are first employed to perform MR active tracking in 3D for robot control. Both were embedded in the needle guide (Fig. 8(a)). 3D fast spoiled gradient recalled-echo (FSPGR) sequence was used to assess the location and orientation of the needle guide. The sequence parameters are stated in Table II**.** A phantom needle made of carbon fiber was then inserted and scanned with the same imaging sequence. Fig. 8(b) shows the resultant MR image in coronal view. Both the coils and the inserted needle can be visualized. The signal intensities of two coils are 1133.00 and 1341.00, in the high contrast to those two circular areas comprising 59 pixels, which are sampled on the background and agar-gel brain, respectively, with

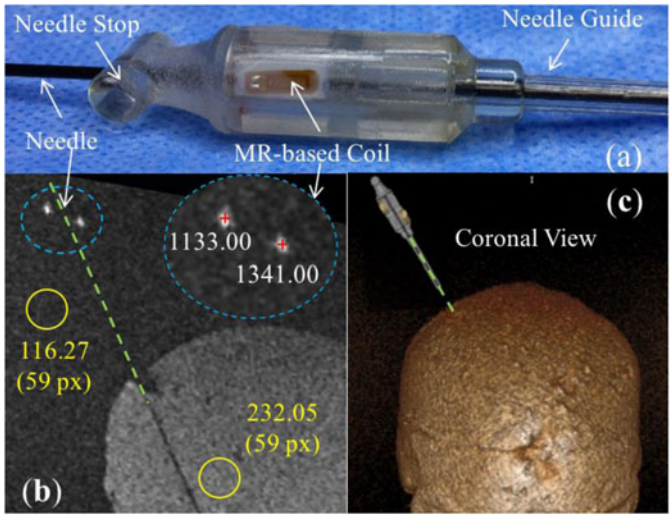

Fig. 8. (a) Needle guide embedded with two MR-based tracking coil units, one of which is shown on its side wall. (b) MR image of the brain phantom (in the coronal view) revealing the two tracking markers by the corresponding bright spots. Dark straight line is the negative artifact of the needle. The two spots are zoomed in (enclosed in the blue dash ellipse). Two red crosses probing at the spots indicate the signal intensity of the coils, in contrast to those intensities average within other two yellow circles: on the background and agar-gel brain phantom. (c) Virtual configurations of the instrument augmented on those high-contrast markers, which is posed above the 3D reconstructed brain phantom. Any change of the instrument pose could be detected continuously (at 30-40Hz) under the real-time MR-tracking sequence.

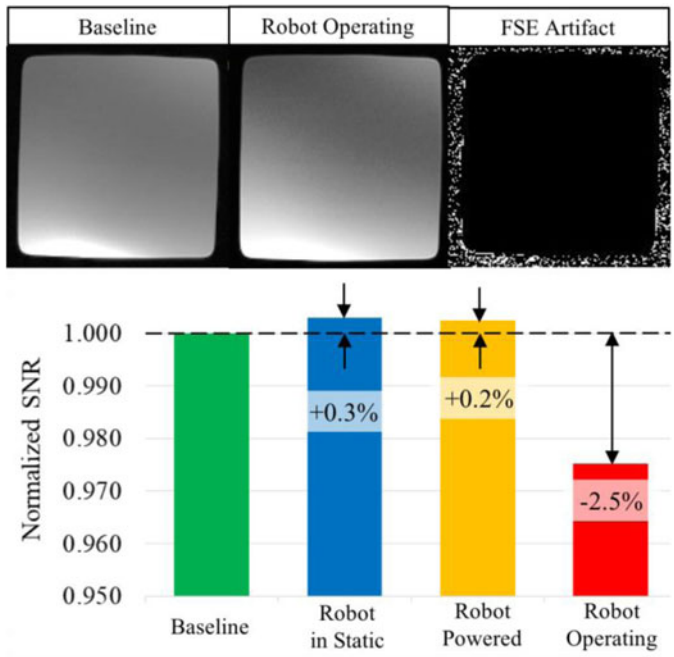

Fig. 9. Upper: T2-weighted FSE images of an SNR phantom. These images were generated at different stages of robot operation. A binary map for FSE sequence marked the actifacts as white pixels. No artifact was observed within the phantom area. As defined by the ASTM standard, it indicated zero artifact was created by the operation of robot. Lower: SNR test results. The existence or operation of the proposed robot is demonstrated to have minimal influence to SNR.

average signal intensities of 116.27 and 232.05. This contrast can be further enhanced by dedicated excitation at lower flip angles (e.g., 1°), which can minimize the background signals. At a distance of 48 mm from the isocenter, the maximum error in marker position was 0.50 mm with inherent precision of 0.12 mm. This deviation can be increased when the marker is further from the isocenter due to the nonlinearities of gradient fields.

D. MRI-Compatibility Test

The MRI-compatibility test was conducted in a 1.5T MRI scanner (SIGNA HDxt, GE Healthcare, USA) at a room temperature of around 20°C. A square SNR phantom (Part Number: 150027, USA Instruments, Inc.) for GE MRI was placed at the isocenter of the scanner. A baseline image without the presence of robot was acquired using T2-weighted fast spin echo (FSE) sequence (Table II). This is the acquisition sequence commonly used for localization in stereotactic neurosurgery. Upon introducing the robot right beside the phantom, MR images were obtained under three different robot operating conditions (Fig. 9), which were: **i)** *Static*: robot was introduced and remained powered off; **ii)** *Powered*: robot remained still, but the hydraulic and electric power was on; **iii)** *Operating*: robot was in full operation. Referring to the guidelines provided by National Electrical Manufacturer's Association (NEMA) [33], the signal-to-noise ratios (SNR) in MR images were evaluated. As the results shown (Fig. 9), SNR loss is within 3% even with the robot in full motion. MR image artifacts caused by the presence of robot were quantified based on the ASTM standard test method [34]. The images corresponding to the two conditions, baseline and robot operating, were compared. Pixels with intensity that varied by 30% or above were considered as artifacts [35]. These artifacts would appear as white pixels in the binary map (FSE Artifact, Fig. 9). No artifact is observed within the phantom area. As defined by the ASTM standard, it indicates the operation of robot generated zero artifact.

IV. Conclusion

In this letter, we present the design of an MRI-guided robot for stereotactic neurosurgery. Not only is the robot capable to perform bilateral targeting of both STNs independently, but also it is compact in size so as to operate within the confined space of a regular MRI head coil. High-performance hydraulic transmissions are incorporated. Maximum stiffness coefficient of 24.35 N/mm can be achieved. A needle insertion task of DBS has also been simulated, in which our experimental results show the targeting accuracy more sufficient than the standard surgical requirement.

The navigation test has been conducted under MRI settings. Advanced MR-based *wireless* tracking is newly developed and incorporated into this robot. Two tracking units are fabricated and embedded inside the instrument guide, marking two very high-contrast bright spots in the image domain. Such marker intensities appear about 10 times of the imaging background and 5 times of the agar-gel brain phantom, thus enabling the accurate and easy instrument localization. It is worth noting that the presented MR-tracking approach could enable a continuous and

real-time positional feedback at 30 40 Hz using the proper MR tracking sequences, thus outperforming the use of many passive fiducials only detected using imaging sequence ones. Moreover, compared to the MR-based active tracking, this *wireless* one does not require any cable connection with the scanner receivers. This avoids many technical complications in wiring the co-axial cables with the tracking units as well. MRI-compatibility test shows the minimal imaging interference is generated even when the robot is in full operation.

In stereotactic neurosurgery, the accuracy of instrument placement can be greatly enhanced by coping with brain shift referring to the brain map continuously updated with the intra-op MRI. This brain shift effect could be minimal with this bilateral approach without having to create extra anchorage site on skull. This development of MR safe robotic system, along with the MR-tracking, is timely while taking advantages of current advances of fast MR imaging/tracking sequences. Direct visualization of surgical targets based on this tele-manipulation of the instrument *in situ* under MRI may prevent the risks from damaging the critical brain structures. This would also avoid the complications of local anesthesia, thus adding confidence by having the post-procedural evaluations of surgical outcome based on images, instead of verbal/physical interaction with the awake patient during the procedure in many current practices. Finally, it is expected to greatly save the operation time from the repeated instrument placement/adjustment, as well as the image alignment with head frame. The overall healthcare expenditure could be significantly reduced, also compensating the high cost of using MRI.

REFERENCES

[1] R. M. deSouza, E. Moro, A. E. Lang, and A. H. Schapira, "Timing of deep brain stimulation in Parkinson disease: A need for reappraisal," *Ann. Neurol.*, vol. 73, pp. 565–575, 2013.

[2] R. A. Vega, K. L. Holloway, and P. S. Larson, "Image-guided deep brain stimulation," *Neurosurg. Clin.*, vol. 25, pp. 159–172, 2014.

[3] C. Nimsky, O. Ganslandt, P. Hastreiter, and R. Fahlbusch, "Intraoperative compensation for brain shift," *Surg. Neurol.*, vol. 56, pp. 357–364, 2001.

[4] C. Sidiropoulos *et al.*, "Intraoperative MRI for deep brain stimulation lead placement in Parkinson's disease: 1 year motor and neuropsychological outcomes," *J. Neurol.*, vol. 263, pp. 1226–1231, 2016.

[5] G. R. Sutherland, Y. Maddahi, L. S. Gan, S. Lama, and K. Zareinia, "Robotics in the neurosurgical treatment of glioma," *Surg. Neurol. Int.*, vol. 6, (Suppl 1): S1, 2015.

[6] J. W. Motkoski and G. R. Sutherland, "Why robots entered neurosurgery," *Exp. Neurosurg. Animal Models*, vol. 116, pp. 85–105, 2016.

[7] M. J. LaRiviere and R. E. Gross, "Stereotactic laser ablation for medically intractable epilepsy: The next generation of minimally invasive epilepsy surgery," *Frontiers Surg.*, vol. 3, no. 64, 2016.

[8] A. H. Hawasli, W. Z. Ray, R. K. Murphy, R. G. Dacey Jr, and E. C. Leuthardt, "Magnetic resonance imaging-guided focused laser interstitial thermal therapy for subinsular metastatic adenocarcinoma: Technical case report," *Oper. Neurosurg.*, vol. 70, pp.332–337, 2011.

[9] W. Wang *et al.*, "Real-time active MR-tracking of metallic stylets in MR-guided radiation therapy," *Magn. Reson. Med.*, vol. 73, pp. 1803–1811, 2015.

[10] C. J. Nycz *et al.*, "Mechanical validation of an MRI compatible stereotactic neurosurgery robot in preparation for pre-clinical trials," in *Proc. IEEE/RSJ Int. Conf. Intell. Robots Syst.,* 2017, pp. 1677–1684.

[11] F. W. Petraglia *et al.*, "Comparison of bilateral vs. staged unilateral deep brain stimulation (DBS) in Parkinson's disease in patients under 70 years of age," *Neuromodulation, Technol. Neural Interface*, vol. 19, pp. 31–37, 2016.

[12] G. Widmann, "Image-guided surgery and medical robotics in the cranial area," *Biomed. Imag. Intervention J.*, vol. 3, no. 1, 2007.

[13] F. Galassi, D. Brujic, M. Rea, N. Lambert, N. Desouza, and M. Ristic, "Fast and accurate localization of multiple RF markers for tracking in MRI-guided interventions," *Magn.Reson. Mater. Phys. Biol. Med.*, vol. 28, pp. 33–48, 2015.

[14] Z. Guo, Z. Dong, K.-H. Lee, H. C. Fu, C. L. Cheung, and K.-W. Kwok, "Robotic stereotactic system for MRI-guided neurosurgery," U.S. Patent 62/623280, 2018.

[15] P. S. Larson, P. A. Starr, G. Bates, L. Tansey, R. M. Richardson, and A. J. Martin, "An optimized system for interventional magnetic resonance imaging-guided stereotactic surgery: Preliminary evaluation of targeting accuracy," *Operative Neurosurg.*, vol. 70, pp. 95–103, 2011.

[16] D. Tarsy, J. L. Vitek, and A. M. Lozano, *Surgical Treatment of Parkinson's Disease and Other Movement Disorders*. Berlin, Germany: Springer, 2002.

[17] *Standard Practice for Marking Medical Devices and Other Items for Safety in the Magnetic Resonance Environment*, ASTM Int., West Conshohocken, PA, USA, Standard ASTM F2503-13, 2013.

[18] G. Ganesh, R. Gassert, E. Burdet, and H. Bleuler, "Dynamics and control of an MRI compatible master-slave system with hydrostatic transmission," in *Proc. IEEE Int. Conf. Robot. Autom.*, 2004, pp. 1288–1294.

[19] D. B. Comber, E. J. Barth, and R. J. Webster, "Design and control of an magnetic resonance compatible precision pneumatic active cannula robot," *J. Med. Devices*, vol. 8, 2014, Art. no. 011003.

[20] Z. Guo, T. Lun, Y. Chen, H. Su, D. Chan, and K. Kwok, "Novel design of an MR-safe pneumatic stepper motor for MRI-guided robotic interventions," in *Proc. 9th Hamlyn Symp. Med. Robot.*, 2016, pp. 50–51.

[21] Y. Chen, K.-W. Kwok, and Z. T. H. Tse, "An MR-conditional high-torque pneumatic stepper motor for MRI-guided and robot-assisted intervention," *Ann. Biomed. Eng.*, vol. 42, pp. 1823–1833, 2014.

[22] J. P. Whitney, T. Chen, J. Mars, and J. K. Hodgins, "A hybrid hydrostatic transmission and human-safe haptic telepresence robot," in *Proc. IEEE Int. Conf. Robot. Autom.*, 2016, pp. 690–695.

[23] K. H. Lee *et al.*, "MR safe robotic manipulator for MRI-guided intracardiac catheterization," *IEEE/ASME Trans. Mechatronics*, 2018.

[24] J.-P. Merlet, "Parallel robots: Open problems," in *Robotics Research*. New York, NY, USA: Springer, 2000, pp. 27–32.

[25] L. Campos, F. Bourbonnais, I. A. Bonev, and P. Bigras, "Development of a five-bar parallel robot with large workspace," in *Proc. ASME 2010 Int. Design Eng. Tech. Conf. Comput. Inf. Eng. Conf.*, 2010, pp. 15–18.

[26] A. Figielski, I. A. Bonev, and P. Bigras, "Towards development of a 2-DOF planar oparallel robot with optimal workspace use," in *Proc. IEEE Int. Conf. Syst. Man Cybern.*, 2007, pp. 1562–1566.

[27] Ö. Bebek, M. J. Hwang, and M. C. Cavusoglu, "Design of a parallel robot for needle-based interventions on small animals," *IEEE/ASME Trans. Mechatronics*, vol. 18, no. 1, pp. 62–73, Feb. 2013.

[28] H. Busse, R. Trampel, W. Gründer, M. Moche, and T. Kahn, "Method for automatic localization of MR-visible markers using morphological image processing and conventional pulse sequences: Feasibility for image-guided procedures," *J. Magn. Reson. Imag.*, vol. 26, pp. 1087–1096, 2007.

[29] Y. Chen *et al.*, "Design and fabrication of MR-tracked metallic stylet for gynecologic brachytherapy," *IEEE/ASME Trans. Mechatronics*, vol. 21, no. 2, pp. 956–962, Apr. 2016.

[30] M. A. Rube, A. B. Holbrook, B. F. Cox, J. G. Houston, and A. Melzer, "Wireless MR tracking of interventional devices using phase-field dithering and projection reconstruction," *Magn. Reson. Imag.*, vol. 32, pp. 693–701, 2014.

[31] M. B. Ooi, M. Aksoy, J. Maclaren, R. D. Watkins, and R. Bammer, "Prospective motion correction using inductively coupled wireless RF coils," *Magn. Reson. Med.*, vol. 70, pp. 639–647, 2013.

[32] Z. Guo, Z. Dong, K.-H. Lee, C. L. Cheung, K. C. D. FU, and K. W. Kwok, "Robotic catheter system for MRI-guided cardiovascular interventions," U.S. Patent 15/630 406; PCT/CN 2017/089 701, 2017.

[33] *Determination of Signal-To-Noise Ratio (SNR) in Diagnostic Magnetic Resonance Images*, Nat. Elect. Manuf. Assoc., Rosslyn, VI, USA, NEMA MS 1-2008 (R2014), 2008.

[34] *Standard Test Method for Evaluation of MR Image Artifacts From Passive Implants* ASTM Int., West Conshohocken, PA, USA, ASTM F2119-07, 2006.

[35] M. A. Tavallaei, M. Lavdas, D. Gelman, and M. Drangova, "Magnetic resonance imaging compatible remote catheter navigation system with 3 degrees of freedom," *Int. J. Comput. Assisted Radiol. Surg.*, vol. 11, pp. 1537–1545, 2016.